

# Design and performance of an X-ray scanning microscope at the Hard X-ray Nanoprobe beamline of NSLS-II

E. Nazaretski,<sup>a</sup> H. Yan,<sup>a</sup> K. Lauer,<sup>a,b</sup> N. Bouet,<sup>a</sup> X. Huang,<sup>a</sup> W. Xu,<sup>a</sup> J. Zhou,<sup>a</sup> D. Shu,<sup>c</sup> Y. Hwu<sup>d</sup> and Y. S. Chu<sup>a\*</sup>

Received 6 June 2017  
Accepted 28 July 2017

<sup>a</sup>Brookhaven National Laboratory, Upton, NY 11973, USA, <sup>b</sup>SLAC National Accelerator Laboratory, Menlo Park, CA 94025, USA, <sup>c</sup>Advanced Photon Source, Argonne National Laboratory, Argonne, IL 60439, USA, and <sup>d</sup>Institute of Physics, Academia Sinica, Taipei 11529, Taiwan. \*Correspondence e-mail: ychu@bnl.gov

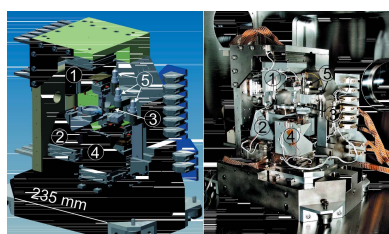
Edited by S. M. Heald, Argonne National Laboratory, USA

**Keywords:** X-ray microscopy; multilayer Laue lenses; nanoprobes.

A hard X-ray scanning microscope installed at the Hard X-ray Nanoprobe beamline of the National Synchrotron Light Source II has been designed, constructed and commissioned. The microscope relies on a compact, high stiffness, low heat dissipation approach and utilizes two types of nanofocusing optics. It is capable of imaging with  $\sim 15 \text{ nm} \times 15 \text{ nm}$  spatial resolution using multilayer Laue lenses and  $25 \text{ nm} \times 26 \text{ nm}$  resolution using zone plates. Fluorescence, diffraction, absorption, differential phase contrast, ptychography and tomography are available as experimental techniques. The microscope is also equipped with a temperature regulation system which allows the temperature of a sample to be varied in the range between 90 K and 1000 K. The constructed instrument is open for general users and offers its capabilities to the material science, battery research and bioscience communities.

## 1. Introduction

X-ray microscopy is a mature characterization tool routinely applied to elucidate various questions in science, technology and engineering (Shapiro *et al.*, 2014; Holler *et al.*, 2017; Yan *et al.*, 2016). The high penetration power of X-rays allows for employing different characterization methods and revealing elemental composition, crystalline phases, strain distribution, oxidation states *etc.* in macroscopic and microscopic samples. To obtain comprehensive chemical and structural information at the nanometer scale, an X-ray microscope has to be equipped with adequate capabilities and acquire multiple datasets simultaneously. Full-field or scanning X-ray microscopes typically serve this purpose and compliment each other (Liu *et al.*, 2016). A number of X-ray scanning microscopes and nanoprobes have been designed, constructed and commissioned in recent years (Winarski *et al.*, 2012; Somogyi *et al.*, 2015; Chen *et al.*, 2014). Different types of nanofocusing optics can be used to achieve nanometer-scale spatial resolution imaging, *e.g.* Fresnel zone plates (ZPs), Kirkpatrick–Baez (KB) mirrors and waveguides (Mohacsi *et al.*, 2017; Chao *et al.*, 2012; Mimura *et al.*, 2010; Krüger *et al.*, 2012; Silva *et al.*, 2017). During the last decade, multilayer Laue lenses (MLLs) were introduced as an alternative to ZPs; they are capable of achieving high focusing efficiency in the hard X-ray regime (Kang *et al.*, 2008; Conley *et al.*, 2016; Morgan *et al.*, 2015; Kubec *et al.*, 2017*a,b*; Yan *et al.*, 2011, 2014), and sub-15 nm focusing has been recently demonstrated (Huang *et al.*, 2013; Morgan *et al.*, 2015). In this work we present a hard X-ray scanning microscope, designed, constructed and installed at



the Nanoprobe beamline of National Synchrotron Light Source II (NSLS-II). The microscope utilizes both MLLs (as high-resolution nanofocusing optics) and a ZP for high-throughput modest-resolution imaging. The instrument supports fluorescence, tomography, differential phase contrast, diffraction and ptychography as imaging techniques and is open for general users.

## 2. Nanofocusing optics and modular concept of the microscope

MLLs were proposed as an alternative approach to achieve nanofocusing and overcome the well known ‘aspect ratio problem’ of ZPs when ZPs are used in the hard X-ray regime. A single MLL optic can be considered as a one-dimensional ZP which needs to satisfy the Bragg condition in order to perform line focusing. Moreover, it exploits the dynamical diffraction effect to achieve high numerical aperture and efficiency unattainable for conventional ZPs (Yan *et al.*, 2007). A pair of linear MLLs needs to be aligned orthogonally with respect to each other to achieve point focusing. In total, eight degrees of motion (five linear and three rotational) are required to perform full alignment. Fig. 1(a) shows a schematic of the MLL microscope. Orthogonality of two lenses plays a critical role in achieving ultimate performance. Angular misalignment introduces an additional cross-phase term in the wavefront causing blurring of the focus. To quantify the degree of misalignment, a requirement has been established that  $\gamma < \lambda f / 2D^2$ , where  $\lambda$  is the wavelength,  $f$  is the focal distance and  $D$  is the aperture of a lens. In order to achieve a 10 nm point focus, the misalignment  $\gamma$  should remain below  $0.01^\circ$  for a typical MLL with a focal length of 4 mm at 12 keV photon energy and an aperture size  $D$  of  $40 \mu\text{m}$ . When fully aligned, both lenses have to maintain their respective angular positions throughout an experiment. Moreover, lateral positions of both lenses along the beam have to be maintained due to a finite depth of focus determined by the photon energy. The two lenses should also be aligned within the depth of focus along the longitudinal direction, which is  $\sim 4 \mu\text{m}$  at 12 keV (Yan *et al.*, 2008). A schematic of a ZP scanning microscope is shown in Fig. 1(b) (the ZP central beamstop is not shown). Since a ZP is already a two-dimensional focusing element, it does not require a sophisticated alignment scheme as in the case of a MLL. Moreover, focal distances for ZPs (depending on the photon energy and

outermost zone width) may vary between 5 and 50 mm as opposed to sub-5 mm focal distances of the MLL optics. Significant differences in alignment schemes and the focal distances of ZPs and MLLs led to the development of two independent scanning microscopes, accommodated within the same vacuum chamber, as shown in Fig. 2.

High resolution (MLL microscope module) and moderate resolution (ZP microscope module) reside on top of a common invar table inside the vacuum chamber (see Fig. 2a). Both modules are mobile and can be manually brought into the beam without disconnecting any cables or optical fibers. Both modules are designed in such a way that they can accommodate the same set of fluorescence detectors (Vortex ME-3 and Bruker XFlash FlatQUAD 5060F) when brought into a working position downstream in the vacuum chamber. During operation, the other module is parked upstream and out of the beam, as shown in Fig. 2(b). The vacuum chamber is equipped with three access doors which allow easy manipulation and re-positioning of both modules. The downstream door provides access for mounting of samples. It is equipped with a large 0.5 mm-thick Be window and allows diffraction measurements in the range  $-5^\circ$  to  $65^\circ$  both vertically and horizontally. The vacuum chamber resides on top of a granite slab ( $\sim 4$  tons) installed in a vibration-isolated and tempera-

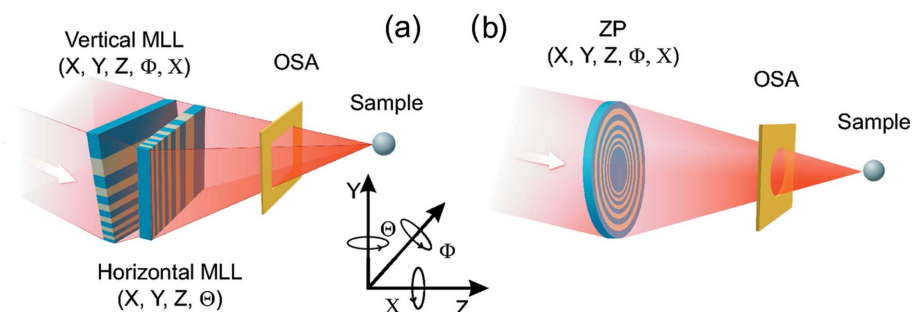


**Figure 1** Two types of nanofocusing optics implemented in the HXN microscope. (a) MLLs and (b) ZP optics. For MLLs, two linear optics have to be aligned orthogonally with respect to each other to achieve point focusing. The degrees of motion required to perform optics alignment and manipulation are depicted.

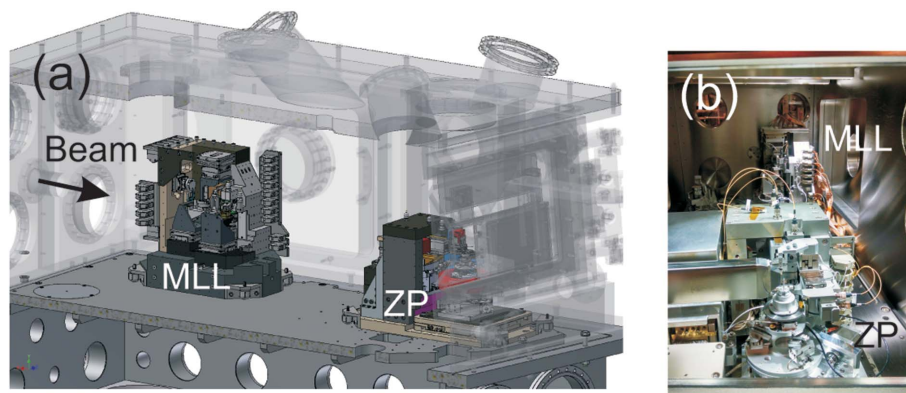


**Figure 2** (a) Demonstration of the modular concept of the instrument. MLL and ZP microscope modules are shown inside the vacuum chamber. (b) Photograph of the two modules. The ZP microscope module is at the front and the MLL module is parked in the back (upstream) of the chamber.

ture-controlled experimental hutch of the hard X-ray nano-probe (HXN) beamline.

### 3. High-resolution MLL microscope module

The design of the MLL microscope module greatly relies on the principles used in scanned probe microscopy systems which employ small form-factor, low heat dissipation and stiff piezo actuators to achieve long-term stability and fine spatial resolution (Mesaros *et al.*, 2011; Nazaretski *et al.*, 2009; Lämmle *et al.*, 2010). Critical components of the MLL microscope module were prototyped and characterized beforehand (Shu *et al.*, 2011; Nazaretski *et al.*, 2013; Kim *et al.*, 2013), with a number of instruments being constructed and validated during the R&D phase of the NSLS-II construction project (Nazaretski *et al.*, 2013, 2014; Shu *et al.*, 2013; Hwu *et al.*, 2013). Development work culminated in the design and construction of the MLL microscope module shown in Fig. 3. Fig. 3(a) depicts the computer-aided design (CAD) model of

the module with all key components enumerated. Fig. 3(b) is a photograph showing the instrument being installed inside the vacuum chamber of the HXN microscope. The instrument consists of different sub-components (assemblies) which perform well defined functions, *i.e.* vertical MLL assembly (1), horizontal MLL assembly (2), order-sorting aperture (OSA) assembly (3) and sample stage assembly (4). All functional modules comprise standard and customized piezo-driven actuators with optimized parameters of travel ranges, form factors and stiffnesses. Nine fiber-optic interferometer heads (5) are used to monitor and control lateral displacements of the vertical and horizontal MLLs and the sample stage. All interferometer heads are mounted on a monolithic invar reference frame to minimize thermal drifts of the critical components. Upon completion, the MLL microscope module was thoroughly characterized in the R&D laboratories of NSLS-II followed by extensive X-ray performance evaluation at beamline I-13 of Diamond Light Source. More technical details describing the design, control and initial performance of the instrument can be found elsewhere (Nazaretski *et al.*, 2015).

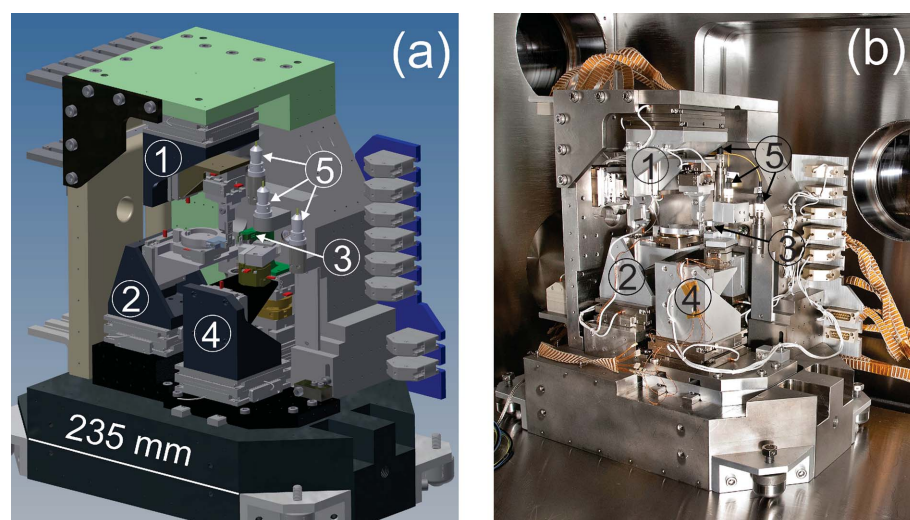


**Figure 3**  
(a) CAD model of the MLL module. Key components are enumerated: 1, Vertical MLL assembly; 2, horizontal MLL assembly; 3, OSA assembly; 4, sample stage assembly; 5, fiber optic interferometers heads. (b) Photograph of the assembled module inside the vacuum chamber.

Fig. 4(a) demonstrates the vibration spectrum of a fully loaded sample module inside the vacuum chamber of the HXN microscope. The main resonance frequencies are between 160 and 170 Hz with a typical amplitude of  $\sim 1.5$  nm. For comparison, resonance frequencies of the vertical and horizontal MLL optics assemblies are in the range 320–350 Hz and reveal sub-nanometer vibrational amplitudes. The vibrational performance of the MLL microscope module allows reliable fly-scan measurements with 5 nm pixel size to be executed. Figs. 4(b) and 4(c) demonstrate the scanning electron microscope (SEM) and X-ray fluorescence (XRF) measurements of a Pt test pattern. Scanning X-ray measurements were performed on a platinum *L*-edge,

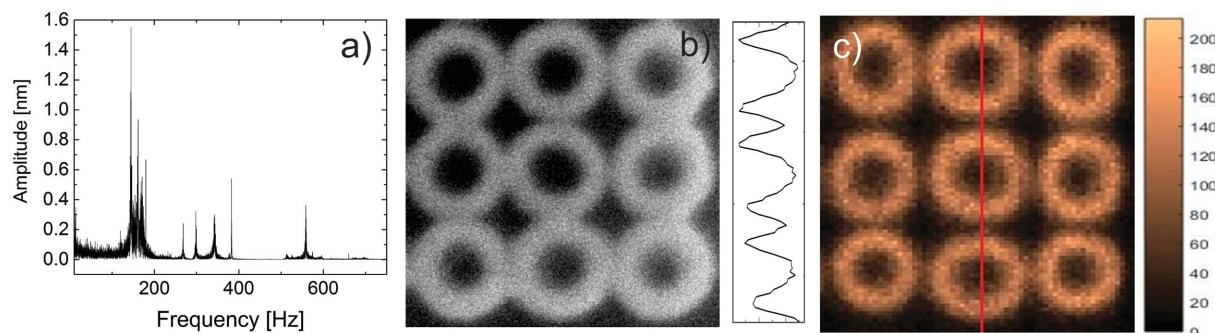


**Figure 4**  
(a) Fast Fourier transform (FFT) spectrum of the fully loaded sample stage in the *x* direction. All resonances are above 100 Hz. (b) SEM image of the Pt test pattern. Donuts are 80 nm in diameter and 20 nm line width. The height of the rings is 200 nm. (c) XRF image (platinum *L*-edge) of the same test pattern, with X-ray energy 12 keV, exposure time 0.2 s and 5 nm per pixel. A scan profile along the vertical line is shown on the left and demonstrates the achieved spatial resolution.

X-ray energy of 12 keV, exposure time of 0.2 s and 5 nm pixel size. Pt circles are 80 nm in diameter, have 20 nm-thick walls and are 200 nm tall. A cross section through a test pattern (see Fig. 4c) shows individual rings with the spacing between them (less than 20 nm) being well resolved indicating a resolution better than 15 nm × 15 nm. The demonstrated resolution is the convolution of a probe and a high-aspect-ratio test pattern. Detailed analysis of the focused beam size and exact imaging resolution will be presented elsewhere. We also measured the focused flux, which equalled  $5 \times 10^8$  photons s<sup>-1</sup> at 12 keV photon energy and 150 mA current in the storage ring. Thermal drifts can cause distortion of acquired fluorescence images if data acquisition spans over an extended period of time. We performed characterization measurements by repeatedly imaging the very same Pt test pattern with a 3 h delay between the measurements. Inferred characteristic thermal drifts do not exceed 5 nm h<sup>-1</sup> in both vertical and horizontal directions.

#### 4. Moderate-resolution ZP microscope module

The design of the ZP microscope module follows a similar concept and utilizes piezo-driven and compact actuators, low heat dissipation components, interferometric monitoring and control. Fig. 5 demonstrates the CAD model and photographs of the module; all key components are labeled. Four ZPs can be mounted on the ZP carriage simultaneously, allowing accommodation of various resolution optics; the outermost zone width and diameter of the used ZPs vary in the range from 25 nm to 50 nm and from 150 μm to 300 μm, respectively. A long-travel-range piezo-driven motion stage allows positioning of the ZPs along the X-ray beam covering the photon energy range from 5 to 25 keV. Long gold-plated reflectors (flatness better than λ/10) are mounted on the ZP carriage and allow interferometric motion and position control of the nanofocusing optics. Similarly to the MLL microscope module, interferometer heads of the ZP microscope module are attached to the invar reference frame surrounding the ZP carriage and the sample stage. ZPs are staggered and can be moved in and out of the beam during an experiment. A

motorized central beam stop assembly is used to accommodate two beam stops of different diameters and is located upstream from the ZP assembly.

The sample assembly consists of a base piezo-crawling stage, a rotary stage, a parallel kinematic device and a sample scanner. The base invar stage has a low profile and a travel range of 20 mm in the X and Z directions; it is used to align the center of the rotary stage with respect to the incoming X-ray beam. The rotary stage has been tested using a characterization system described elsewhere (Xu *et al.*, 2014) and demonstrated <1 μm combined rotational errors at 50 mm above its top plate. The parallel kinematic device has a low profile (its height is only 45 mm) and is used to bring the sample to the center of rotation. It is also used to perform angular adjustments for diffraction measurements. The sample scanner has a 40 μm travel range in the X, Y and Z directions. It is equipped with external capacitive and interferometric sensors for position encoding. Interferometers are primarily used for two-dimensional scanning and characterization measurements while capacitive sensors are activated during three-dimensional tomographic measurements. The OSA assembly consists of X, Y, Z motion elements which are integrated into the invar reference frame and can follow the sample for optimal performance. Vibrational characteristics of the sample stage in the X direction are shown in Fig. 6(a). There are a number of broadened resonance peaks ranging from 100 Hz to 500 Hz, with characteristic amplitudes of less than 0.5 nm. These resonances originate from a number of stages underneath the scanner. The scanner itself has a resonance frequency of ~415 Hz. Since the ZP microscope module is used for moderate spatial resolution imaging experiments few nanometer integrated vibrational amplitudes do not affect the quality of the acquired data. Figs. 6(b)–6(d) demonstrate the focusing performance of the ZP microscope module. The scanning probe imaging experiment was conducted at 8 keV photon energy. A star test pattern was scanned at a slightly de-focused plane of the ZP with a 25 nm outermost zone width and 150 μm diameter. The scan trajectory followed a Fermat spiral pattern covering a 2 μm × 2 μm field of view with 50 nm circular increment step. At each scan

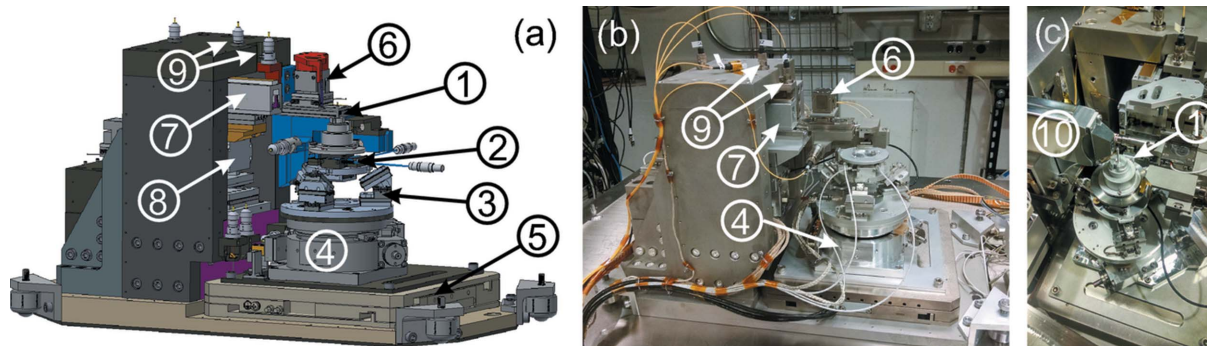


**Figure 5** (a) CAD model of the ZP microscope module. Key components are enumerated. 1, Sample mount; 2, sample scanner with capacitive position readout; 3, parallel kinematic Smarpod device; 4, sample rotary stage; 5, sample base stages; 6, OSA assembly; 7, ZP carriage; 8, ZP manipulation assembly; 9, fiber optics interferometers. (b) Photograph of the ZP microscope module. (c) Photograph of the ZP microscope module with the sample mounted. 10, Fluorescence detector.

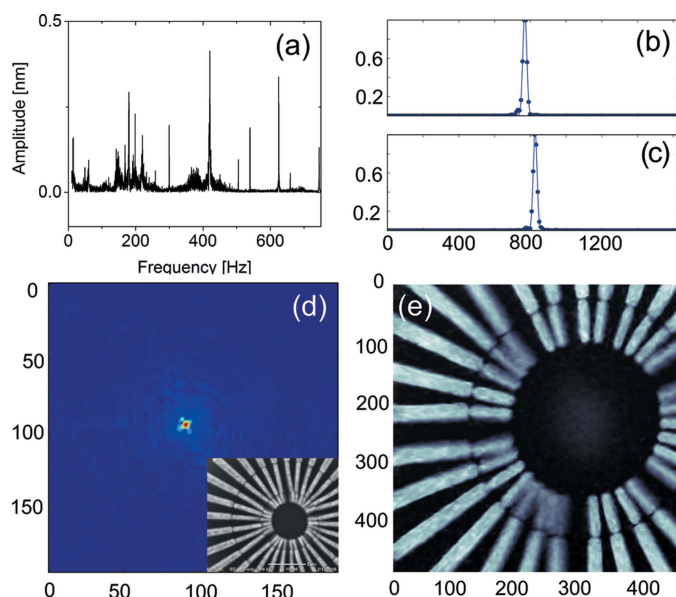


**Figure 6**

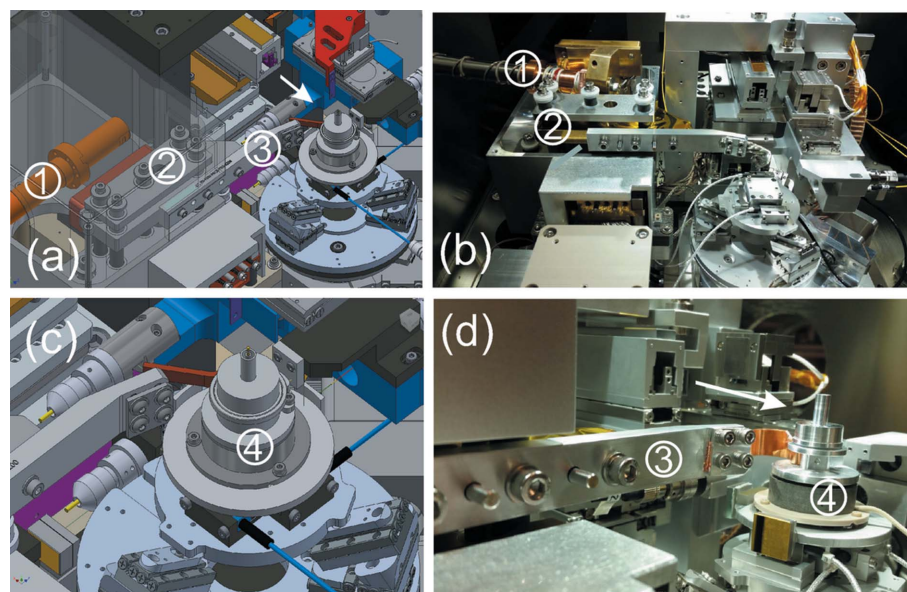
(a) FFT spectrum of the sample stage in the *X* direction. (b, c) Gaussian fittings of horizontal and vertical line plots give full width at half-maximum focus sizes of 26 nm and 25 nm, respectively. (d) The reconstructed focused beam. (e) The reconstructed phase of a star test pattern. The width of the finest inner spokes is 100 nm. Some of the inner spokes have collapsed (the thickness of an Au test pattern is 800 nm), which can also be seen in the SEM image, shown as an inset in (d).

position the far-field diffraction data were collected by a Merlin pixel area detector with 55  $\mu\text{m}$  pixel size, placed 0.58 m away from the sample. A  $192 \times 192$  array frame was cropped to feed into the ptychography reconstruction process using a difference map engine, which converges within 100 iterations and gives complex-valued images with 8.5 nm pixel size, as shown in Figs. 6(d) and 6(e). Gaussian fittings of horizontal and vertical line plots give full width at half-maximum focus sizes of 26 nm and 25 nm, respectively. Measurements of the focused flux were conducted for one of the ZPs and revealed  $1.17 \times 10^9$  photons  $\text{s}^{-1}$  per  $50 \text{ nm} \times 50 \text{ nm}$  at 10 keV photon energy and 300 mA current in the storage ring.

## 5. Temperature regulation system

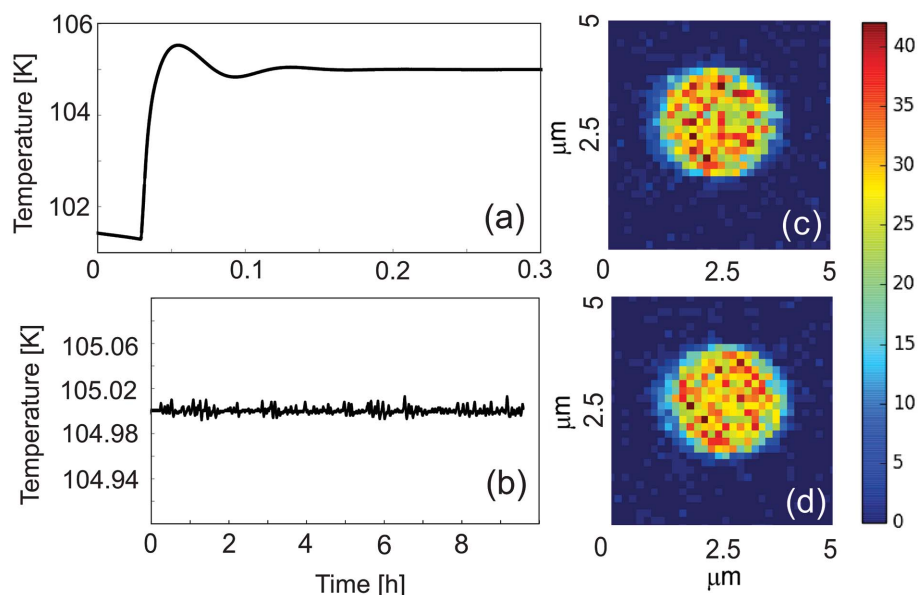
High-spatial-resolution X-ray imaging can greatly benefit from an instrument's ability to vary the pressure, magnetic field or temperature of a sample (Huang *et al.*, 2015; Uhlíř *et al.*, 2013; Deng *et al.*, 2015). Dynamic processes and phase transitions can be explored revealing a full phase diagram of a particular sample. We have developed a temperature regulation system for the ZP microscope module of the HXN micro-

scope which allows a sample's temperature to be changed in the range from 90 K to 1000 K. The system comprises two independent setups: the cooling sample mount is used for the measurements in the temperature range between 90 K and 450 K and the heating sample mount operates in the temperature range 300–1000 K. Fig. 7 demonstrates the CAD models and the photographs of the cooling setup, with all major components listed. A helium (nitrogen-compatible) flow cryostat has been used to provide cooling for a sample mount. The cold finger of the cryostat is connected through a number of vibration isolation posts and braids to the cooling arm. The cooling arm extends to a sample assembly [see Figs. 7(b) and 7(d)] and is linked to the sample mount through oxygen-free high-conductivity (OFHC) copper (or graphite) cooling stripes. Stripes are used to optimize thermal conductivity and minimize stiffness when performing rotation during tomography measurements. The temperature difference between the cryostat tip and the sample mount assembly was measured to be  $\sim 10$  K when using nitrogen for cooling. The sample pin resides on top of a sample mount which is thermally decoupled from a scanning stage. It is protected by a radiation shield in order to minimize the thermal influence on the surrounding microscope components. A combination of ceramic insulators and point contacts is used to provide thermal impedance between the sample mount and the scanner. No significant temperature increase has been observed at the scanner location when a sample is cooled or heated. The nichrome heater and a calibrated thermometer are mounted next to the sample pin and ensure proper temperature regulation. Fig. 8 demonstrates the performance of the temperature regulation system. Fig. 8(a) shows the sample response to a 4 K temperature step. The settling time is



**Figure 7**

(a, c) CAD models of the temperature regulation system. Major components are numbered. 1, Cold finger of a cryostat; 2, vibration isolation platform; 3, cooling arm with attached cooling stripes (copper in this particular case); 4, sample holder assembly. (b, d) Photographs of the installed system; the beam direction is shown with an arrow.


**Figure 8**

(a) Response of the temperature regulation system to a 4 K step at cryogenic temperatures (PID parameters are not fully optimized). (b) Stability of the sample temperature over a 10 h time period. (c, d) Fluorescence images of a Cr dot,  $T = 800$  K, photon energy = 11.95 keV, pixel size = 160 nm. The time delay between data shown in (c) and (d) equals 1560 s.

~10 min; Fig. 8(b) demonstrates the long-term temperature stability. Temperature can be maintained for many hours (100 l nitrogen dewar allows operation for up to one week without refill) with fluctuations of less than 20 mK. Figs. 8(c) and 8(d) illustrate the performance of the high-temperature setup. Chromium dots, 90 nm-thick, deposited on a Si substrate for sample fiducialization were imaged using X-ray fluorescence at 800 K. Two identical scans were acquired 1560 s apart (pixel size 160 nm). When comparing relative positions of two dots by calculating their center of mass, we obtained drifts of 75 nm in the horizontal and 40 nm in the vertical direction, respectively. Cross-correlation calculations reveal a drift of 121 nm horizontally and 46 nm vertically. The system demonstrated good thermal stability; however, to fully quantify nanometer-scale drifts, finer features have to be imaged with an adequate pixel size.

## 6. Conclusion

In conclusion, we have designed, constructed and commissioned a high-resolution versatile scanning microscope suitable for imaging in the hard X-ray regime. The instrument supports fluorescence, diffraction, absorption, differential phase contrast, tomography and ptychography imaging techniques and yields  $\sim 15$  nm  $\times$  15 nm imaging resolution for the MLL microscope module and 25 nm  $\times$  26 nm imaging resolution for the ZP microscope module. The microscope is equipped with a temperature regulation system and allows the temperature of a sample to be varied in the range 90–1000 K. The instrument is installed at the HXN beamline of NSLS-II and is open to the general user community.

## Acknowledgements

This work was performed using resources of the R&D laboratories and the Hard X-ray Nanoprobe (3-ID HXN) beamline of the National Synchrotron Light Source II, a US Department of Energy (DOE) Office of Science User Facility operated for the DOE Office of Science by Brookhaven National Laboratory under Contract No. DE-SC0012704. YH thanks The Innovation and Application of Nanoscience Thematic Program and the Academia Sinica Thematic Project for support during this work.

## Funding information

Funding for this research was provided by: US Department of Energy (DOE) Office of Science User Facility operated for the DOE Office of Science by Brookhaven National Laboratory (contract No. DE-SC0012704); The Innovation and Application of Nanoscience Thematic Program and the Academia Sinica Thematic Project.

## References

- Chao, W., Fischer, P., Tyliczszak, T., Rekawa, S., Anderson, E. & Naulleau, P. (2012). *Opt. Express*, **20**, 9777–9783.
- Chen, S., Deng, J., Yuan, Y., Flachenecker, C., Mak, R., Hornberger, B., Jin, Q., Shu, D., Lai, B., Maser, J., Roehrig, C., Paunesku, T., Gleber, S. C., Vine, D. J., Finney, L., VonOsinski, J., Bolbat, M., Spink, I., Chen, Z., Steele, J., Trapp, D., Irwin, J., Feser, M., Snyder, E., Brister, K., Jacobsen, C., Woloschak, G. & Vogt, S. (2014). *J. Synchrotron Rad.* **21**, 66–75.
- Conley, R., Bouet, N., Chu, Y. S., Huang, X., Kang, H. C., Macrander, A. T., Maser, J., Nazaretski, E., Stephenson, G. B. & Yan, H. (2016). *Synchrotron Radiat. News*, **29**, 16–20.
- Deng, J., Vine, D. J., Chen, S., Nashed, Y. S. G., Jin, Q., Phillips, N. W., Peterka, T., Ross, R., Vogt, S. & Jacobsen, C. J. (2015). *Proc. Natl. Acad. Sci.* **8**, 2314–2319.

- Holler, M., Guizar-Sicairos, M., Tsai, E. H. R., Dinapoli, R., Müller, E., Bunk, O., Raabe, J. & Aeppli, G. (2017). *Nature (London)*, **543**, 402–406.
- Huang, X., Yan, H., Nazaretski, E., Bouet, N., Conley, R., Harder, R., Robinson, I. & Chu, Y. S. (2013). *Sci. Rep.* **3**, 3562.
- Huang, X., Yang, W., Harder, R., Sun, Y., Lu, M., Chu, Y. S., Robinson, I. K. & Mao, H. K. (2015). *Nano Lett.* **15**, 7644–7649.
- Hwu, E., Nazaretski, E., Chu, Y. S., Chen, H.-H., Chen, Y.-S., Xu, W. & Hwu, Y. (2013). *Rev. Sci. Instrum.* **84**, 123702.
- Kang, H., Yan, H., Winarski, R., Holt, M., Maser, J., Liu, C., Conley, R., Vogt, S., Macrander, A. & Stephenson, G. B. (2008). *Appl. Phys. Lett.* **92**, 221114.
- Kim, J., Lauer, K., Yan, H., Chu, Y. S. & Nazaretski, E. (2013). *Rev. Sci. Instrum.* **84**, 035006.
- Krüger, S. P., Neubauer, H., Bartels, M., Kalbfleisch, S., Giewekemeyer, K., Wilbrandt, P. J., Sprung, M. & Salditt, T. (2012). *J. Synchrotron Rad.* **19**, 227–236.
- Kubec, A., Maser, J., Formánek, P., Franke, V., Braun, S., Gawlitza, P., Leson, A. & Macrander, A. (2017a). *Appl. Phys. Lett.* **110**, 111905.
- Kubec, A., Melzer, K., Gluch, J., Niese, S., Braun, S., Patommel, J., Burghammer, M. & Leson, A. (2017b). *J. Synchrotron Rad.* **24**, 413–421.
- Lämmle, K., Trevethan, T., Schwarz, A., Watkins, M., Shluger, A. & Wiesendanger, R. (2010). *Nano Lett.* **10**, 2965–2971.
- Liu, Y., Meirer, F., Krest, C. M., Webb, S. & Weckhuysen, B. M. (2016). *Nat. Commun.* **7**, 12634.
- Mesaros, A., Fujita, K., Eisaki, H., Uchida, S., Davis, J. S., Sachdev, S., Zaanen, J., Lawler, M. J. & Kim, E.-A. (2011). *Science*, **333**, 426–430.
- Mimura, H., Handa, S., Kimura, T., Yumoto, H., Yamakawa, D., Yokoyama, H., Matsuyama, S., Inagaki, K., Yamamura, K., Sano, Y., Tamasaku, K., Nishino, Y., Yabashi, M., Ishikawa, T. & Yamauchi, K. (2010). *Nat. Phys.* **6**, 122–125.
- Mohacsi, I., Vartiainen, I., Rösner, B., Guizar-Sicairos, M., Guzenko, V. A., McNulty, I., Winarski, R., Holt, M. V. & David, C. (2017). *Sci. Rep.* **7**, 43624.
- Morgan, A. J., Prasciolu, M., Andrejczuk, A., Krzywinski, J., Meents, A., Pennicard, D., Graafsma, H., Barty, A., Bean, R. J., Barthelmess, M., Oberthuer, D., Yefanov, O., Aquila, A., Chapman, H. N. & Bajt, S. (2015). *Sci. Rep.* **5**, 9892.
- Nazaretski, E., Graham, K. S., Thompson, J. D., Wright, J. A., Pelekhov, D. V., Hammel, P. C. & Movshovich, R. (2009). *Rev. Sci. Instrum.* **80**, 083704.
- Nazaretski, E., Huang, X., Yan, H., Lauer, K., Conley, R., Bouet, N., Zhou, J., Xu, W., Eom, D., Legnini, D., Harder, R., Lin, C.-H., Chen, Y.-S., Hwu, Y. & Chu, Y. S. (2014). *Rev. Sci. Instrum.* **85**, 033707.
- Nazaretski, E., Kim, J., Yan, H., Lauer, K., Eom, D., Shu, D., Maser, J., Pešić, Z., Wagner, U., Rau, C. & Chu, Y. S. (2013). *Rev. Sci. Instrum.* **84**, 033701.
- Nazaretski, E., Lauer, K., Yan, H., Bouet, N., Zhou, J., Conley, R., Huang, X., Xu, W., Lu, M., Gofron, K., Kalbfleisch, S., Wagner, U., Rau, C. & Chu, Y. S. (2015). *J. Synchrotron Rad.* **22**, 336–341.
- Shapiro, D. A., Yu, Y.-S., Tylliszczak, T., Cabana, J., Celestre, R., Chao, W., Kaznatcheev, K., Kilcoyne, A. L. D., Maia, F., Marchesini, S., Meng, Y. S., Warwick, T., Yang, L. L. & Padmore, H. A. (2014). *Nat. Photon.* **8**, 765–769.
- Shu, D., Maser, J., Chu, Y., Yan, H., Nazaretski, E., O'Hara, S., Kearney, S., Anton, J., Quintana, J. & Shen, Q. (2011). *AIP Conf. Proc.* **1365**, 144.
- Shu, D., Nazaretski, E., Kim, J., Yan, H., Lauer, K., Mullany, B., Kuhne, D., Maser, J. & Chu, Y. S. (2013). *J. Phys. Conf. Ser.* **463**, 012029.
- Silva, J. S. da, Pacureanu, A., Yang, Y., Bohic, S., Morawe, C., Barrett, R. & Cloetens, P. (2017). *Optica*, **4**, 492–495.
- Somogyi, A., Medjoubi, K., Baranton, G., Le Roux, V., Ribbens, M., Polack, F., Philippot, P. & Samama, J.-P. (2015). *J. Synchrotron Rad.* **22**, 1118–1129.
- Uhlř, V., Urbánek, M., Hladík, L., Spousta, J., Im, M.-Y., Fischer, P., Eibagi, N., Kan, J. J., Fullerton, E. E. & Šikola, T. (2013). *Nat. Nanotech.* **8**, 341–346.
- Winarski, R. P., Holt, M. V., Rose, V., Fuesz, P., Carbaugh, D., Benson, C., Shu, D., Kline, D., Stephenson, G. B., McNulty, I. & Maser, J. (2012). *J. Synchrotron Rad.* **19**, 1056–1060.
- Xu, W., Lauer, K., Chu, Y. & Nazaretski, E. (2014). *J. Synchrotron Rad.* **21**, 1367–1369.
- Yan, H., Conley, R., Bouet, N. & Chu, Y. S. (2014). *J. Phys. D*, **47**, 263001.
- Yan, H., Maser, J., Kang, H. C., Macrander, A. & Stephenson, G. B. (2008). *Proc. SPIE*, **7077**, 70770Q.
- Yan, H., Maser, J., Macrander, A., Shen, Q., Vogt, S., Stephenson, G. B. & Kang, H. C. (2007). *Phys. Rev. B*, **76**, 115438.
- Yan, H., Nazaretski, E., Lauer, K., Huang, X., Wagner, U., Rau, C., Yusuf, M., Robinson, I., Kalbfleisch, S., Li, L., Bouet, N., Zhou, J., Conley, R. & Chu, Y. S. (2016). *Sci. Rep.* **6**, 20112.
- Yan, H., Rose, V., Shu, D., Lima, E., Kang, H. C., Conley, R., Liu, C., Jahedi, N., Macrander, A. T., Stephenson, G. B., Holt, M., Chu, Y. S., Lu, M. & Maser, J. (2011). *Opt. Express*, **19**, 15069–15076.